

Titanic magnetoresistance and signature of non-degenerate Dirac nodes in ZrSiS.

R. Singha, A. Pariari, B. Satpati, P. Mandal

Saha Institute of Nuclear Physics, 1/AF Bidhannagar, Kolkata 700 064, India

(Dated: July 22, 2022)

We present the results on magnetotransport properties of ZrSiS single crystals. Extremely large, non-saturating and non-linear magneto-resistance ($\sim 1.4 \times 10^5\%$) is observed at 2 K and 9 T magnetic field. Large anisotropy in magnetoresistance, with field applied along different crystallographic axes, have also been observed. The Shubnikov - de Haas oscillation reflects the presence of a small and a large Fermi pocket. Quantum oscillation along with Hall resistance indicate multiple band crossing at different energy levels of electronic band structure and the contribution of both hole and electron type charge carriers, which is in agreement with the earlier theoretical and ARPES reports. Non trivial π Berry phase confirms the Dirac fermionic nature of charge carriers. Fermi wave vector, Fermi velocity and cyclotron effective mass of the charge carrier have been calculated from the oscillation data.

The search for new topological states of matter is one of the new frontiers in physics. The discovery of topological insulators and subsequent finding of topological Dirac and Weyl semimetals paved the way to study the rich physics involved [1–5]. In Dirac semimetals, the bulk conduction and valence bands cross each other at four-fold degenerate Dirac points protected by time reversal (TRS) and crystal symmetry (CS) [6, 7]. Close to the Dirac points, the bands are linearly dispersing, thus these systems often identified as the 3 dimensional analogue of graphene. Shortly after the theoretical prediction [6, 7], the existence of bulk Dirac points have been verified in Cd_3As_2 and Na_3Bi through ARPES and transport measurements [8–11]. While Dirac points are protected by large number of symmetries, by breaking either TRS or inversion symmetry (IS) each Dirac point can be broken into a pair of doubly degenerate Weyl points accompanied by the surface Fermi arc connecting them.[6, 7] The IS breaking compounds TaAs, NbAs, NbP, TaP [12–16] and TRS breaking YbMnBi_2 [17] have been confirmed to host Weyl fermions. Apart from these compounds, a new type of semimetals, namely the topological nodal line semimetals (TNLSM) have emerged [18–21], where band crossings have been observed along one-dimensional closed lines in \mathbf{k} space instead of discrete points. Although proposed in few materials [19, 22–24], the existence of nodal lines has been experimentally verified only in IS breaking non-centrosymmetric superconducting compound PbTaSe_2 [25, 26], where the nodal rings are protected by reflection symmetry under spin-orbit coupling.

Recently, ARPES measurement and first principle calculations have revealed the existence of multiple Dirac crossings along with an unconventional surface and bulk state hybridization in ZrSiS [27]. The Dirac nodes are protected by non-symmorphic symmetry and reside at different energy values of band structure. The diamond shaped Fermi surface consistent with the band structure calculations has been observed in ARPES measurement. Another feature which, in particular, makes ZrSiS an interesting system is the energy range of the linear band dispersion. While most of the materials observed so far

have linear band dispersion up to few hundred meV from the Dirac point, in ZrSiS the range is seen to be as high as 2 eV in some regions of the Brillouin zone.

Here we report the magnetotransport properties of single crystalline ZrSiS. An extremely large value of magnetoresistance accompanied by Shubnikov-de Haas (SdH) oscillation have been observed and analyzed to calculate the Fermi surface properties of the material.

Single crystals of ZrSiS were grown via iodine vapor transport in a two steps process. At first, the polycrystalline powder was synthesized using elemental Zr (Alfa Aesar 99.9%), Si (Strem Chem. 99.999%), S (Johnson Matthey Chem. 99.9995%) in a process described elsewhere [28]. Then the polycrystalline powder together with iodine in a concentration of 5 mg/cm³ were sealed in a quartz tube under vacuum. The quartz tube was then kept in a gradient furnace for 72 h with the powder at 1100°C, while the cooler end at 1000°C. Shiny rectangular plate like crystals were obtained at the cooler end for transport measurements.

In Fig. 1(a), a typical single crystal of ZrSiS is shown with different crystallographic axis, along which measurements have been done. The crystals cleave perpendicular to \mathbf{c} axis similar to earlier report [27]. High resolution transmission electron microscopy (HRTEM) image of the crystal along \mathbf{ac} plane [Fig. 1(b)] confirms the high quality crystalline nature. The electron diffraction patterns obtained in HRTEM measurement are shown in Fig. 1(c) and 1(d). The stoichiometry of the grown crystals was verified using energy dispersive X - ray spectroscopy [29]. The transport measurements were performed in a 9 T Physical Property Measurement System (Quantum Design) in ac transport option in four probe setup using conducting silver paste and gold wire for electrical contacts.

As shown in Fig. 2, the zero field resistivity measurement shows metallic character, $\rho(T)$ decreases monotonically from $\sim 15 \mu\Omega \text{ cm}$ at 300 K to about 60 K, below which it exhibits a very weak temperature dependence. The resistivity at 2 K becomes as low as $\sim 52 \text{ n}\Omega \text{ cm}$ which is comparable with that of Cd_3As_2 as previously reported [9]. The residual resistivity ratio $\rho(300 \text{ K})/\rho(2$

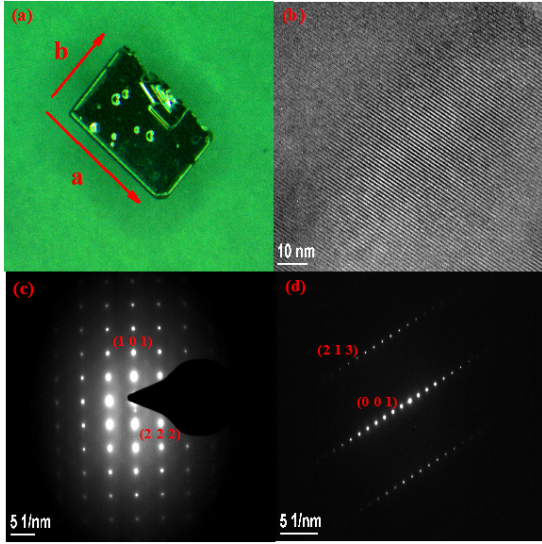


FIG. 1. (a) ZrSiS single crystal with crystal directions. (b) HRTEM image of the crystal. (c) and (d) Selective area electron diffraction (SAED) pattern obtained through HRTEM measurement.

K) is found to be 288, which is quite large and confirms good metallicity and high quality of the crystals. With the application of magnetic field, the low temperature resistivity undergoes a drastic enhancement, thus the nature of the slope of $\rho(T)$ curve changes. As a result, a metal-semiconducting like crossover occurs even at a field of 1 T only. This type of magnetic field induced transition, which often described as a result of gap opening at the band touching points, has already been demonstrated in NbP, WTe₂ and NbSb₂ [14, 30, 31]. It is evident from Fig. 2 that the metal-semiconducting transition is extremely sensitive to the direction of applied field. With current along **a** axis and magnetic field parallel to **c** axis, a strong crossover has been seen. On the other hand, rotating the field direction by 90°, i.e. parallel to **b** axis, results in much weaker metal - semiconductor like crossover, which occurs at higher field strength. This implies an anisotropic electrical transport with magnetic field applied along two different crystallographic axis.

In both the cases, the transition temperature increases monotonically with increasing field. However, for a given magnetic field, the transition temperatures are different for two directions. Considering the thermal activation energy expression as in the case of intrinsic semiconductor [32, 33], $\rho(T) = \rho_0 \exp(E_g/2k_B T)$, we have calculated thermal activation energy gaps of 23.44 meV and 3.56 meV at 9 T for field directions along **c** axis and **b** axis, respectively. The calculated gap E_g shows a magnetic field dependence [29].

The transverse magnetoresistance (MR), i.e. the change in resistance with magnetic field (up to 9 T) applied perpendicular to the current direction has been measured at several temperatures from 2 to 300 K, where MR is defined as, $[(\rho(B) - \rho(0))/\rho(0)] \times 100$

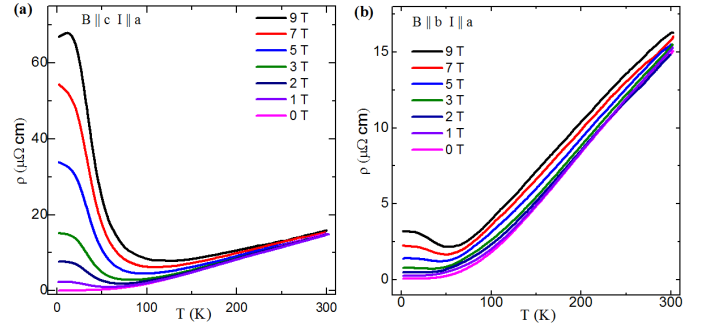


FIG. 2. Temperature dependence of resistivity measured under different transverse magnetic fields when (a) $B \parallel c$ axis, (b) $B \parallel b$ axis.

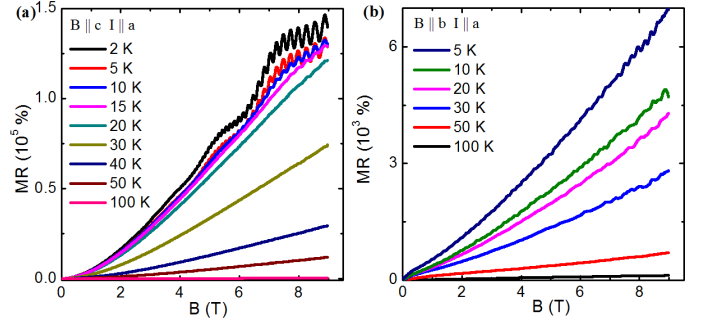


FIG. 3. Transverse magnetoresistance with current along **a** axis and magnetic field parallel to (a) **c** axis and (b) **b** axis, measured at different temperatures, up to 9 T.

%. As shown in Fig. 3 at some representative temperatures, with current parallel to **a** axis and magnetic field along **c** axis, an extremely large, non saturating MR is obtained at low temperatures. At 2 K with a magnetic field 9 T, the calculated MR has a value 1.4×10^5 % which is comparable to that of the Dirac semimetal Cd₃As₂ (MR = 1.6×10^5 % at 2.5 K, 15 T) and Weyl semimetal candidates TaAs (MR = 8×10^4 % at 1.8 K, 9 T), NbP (MR = 8.5×10^5 % at 1.85 K, 9 T), NbAs (MR = 2.3×10^5 % at 2 K, 9 T), WTe₂ (MR = 4.5×10^5 % at 4.5 K, 14.7 T) and NbSb₂ (MR = 1.3×10^5 % at 2 K, 9 T) [12–16, 30, 31, 34]. With the increase in temperature, MR decreases dramatically with a value of just about 14 % at 300 K in 9 T.

It is apparent from the resistivity data that the transverse MR is highly anisotropic in nature. Applying field parallel to **b** axis and keeping the current direction unchanged, the MR has been seen to reduce to ~ 7000 % at 5 K and 9 T. The anisotropy in MR vanishes at 300 K as indicated by a value of 12 % at 9 T. At 3 K with a magnetic field 9 T the anisotropic ratio $\rho(B \parallel c)/\rho(B \parallel b)$ has a large value 21 which is comparable to NbSb₂ (20 at 2 K, 9 T) as previously reported [31].

Another interesting feature which emerges from the transport measurement is the presence of SdH oscillation

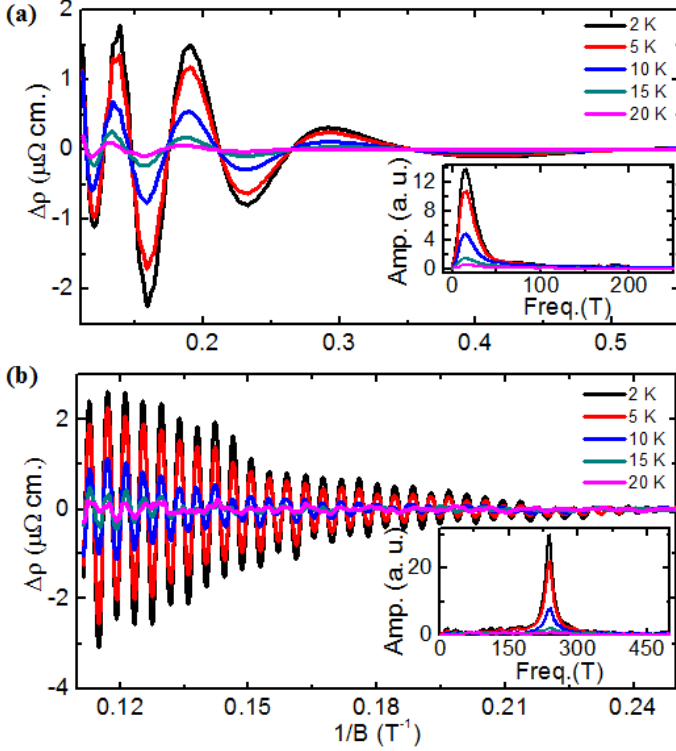


FIG. 4. SdH oscillation obtained by subtracting smooth background from magnetoresistance measurement, plotted with inverse magnetic field ($1/B$) at different temperatures for two deconvoluted components. The insets in both figures show the corresponding FFT results.

traceable at fields even below 2 T and temperature up to 20 K. This not only gives an insight into the nature of the Fermi surface, but also it is an evidence of very high mobility of the charge carriers present in the system. From the oscillatory data, it is clear that there are more than one frequency present. To extract the oscillatory component $\Delta\rho(B)$, a smooth background is subtracted from the field dependent resistivity $\rho(B)$. To deconvolute the two components of oscillation, background subtraction has been done in two steps.

In Fig.4(a) and Fig.4(b), $\Delta\rho(B)$ for two different components is plotted as a function of $1/B$ at some representative temperatures. The fast Fourier transform (FFT) analysis of the components reveal oscillation frequencies 14.15 T and 238.24 T, respectively. Obtained frequencies indicate the existence of a very large and a small Fermi surface cross-sections perpendicular to c axis. Using the Onsager relationship

$$F = (\varphi_0/2\pi^2)A_F \quad (1)$$

where φ_0 is the single magnetic flux quantum and A_F is the Fermi surface cross-section perpendicular to the applied magnetic field, we have calculated cross-sections $1.35 \times 10^{-3} \text{ \AA}^{-2}$ and $22.7 \times 10^{-3} \text{ \AA}^{-2}$ respectively. Considering circular geometry of the cross-section, we obtain Fermi momentum $2.07 \times 10^{-2} \text{ \AA}^{-1}$ and 8.5×10

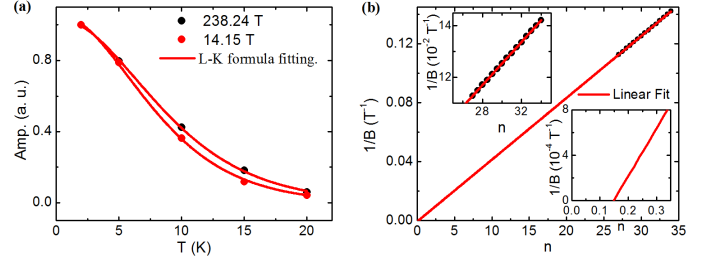


FIG. 5. (a) Temperature dependence of relative amplitude of SdH oscillation for both Fermi pockets. (b) Landau level index plot for 238.24 T frequency oscillation. Upper and lower inset shows the experimental data points and the intercept by extrapolated linear fitting, respectively.

-2 \AA^{-1} , respectively.

In Fig.5(a), the oscillation amplitude is shown as a function of temperature. To determine the cyclotron effective mass of the charge carriers, we have fitted the oscillation amplitude for both frequencies using thermal damping factor in Lifshitz - Kosevich formula,

$$R_T = (2\pi^2 k_B T / \beta) / \sinh(2\pi^2 k_B T / \beta) \quad (2)$$

where $\beta = e\hbar B / m^*$ and m^* is the cyclotron effective mass.

The cyclotron effective masses of the charge carriers are determined to be $\sim 0.14 m_0$ and $\sim 0.1 m_0$ for 238.24 T and 14.15 T frequencies, respectively. m_0 is the rest mass of the free electron. Large values of Fermi velocities ($v_F = \hbar k_F / m^*$), $6.93 \times 10^5 \text{ m/s}$ and $2.37 \times 10^5 \text{ m/s}$ are calculated. To get the carrier density, we have employed the relation with the oscillation frequency [35, 36]

$$\Delta \left(\frac{1}{B} \right) = \frac{2e}{\hbar} \left(\frac{g_s g_v}{6\pi^2 n_{3D}} \right)^{2/3} \quad (3)$$

where g_s and g_v are the spin and valley degeneracies. We calculated carrier densities $2.07 \times 10^{19} / \text{cm}^3$ and $3 \times 10^{17} / \text{cm}^3$ for larger and smaller frequencies respectively. From the magnetic field dependence of oscillation amplitude, $\Delta\rho \propto \exp(-2\pi^2 k_B m^* T_D / \hbar e B)$, Dingle temperatures (T_D) are determined to be 11.18 K and 3.4 K for two oscillation components at 2 K. To get an quantitative estimate about the mobility of the charge carriers in the system, we have calculated the quantum mobility $\mu_q = (e\hbar / 2\pi k_B m^* T_D)$. The obtained values, $\sim 1.35 \times 10^3 \text{ cm}^2 \text{ V}^{-1} \text{ s}^{-1}$ and $\sim 6.2 \times 10^3 \text{ cm}^2 \text{ V}^{-1} \text{ s}^{-1}$ for larger and smaller frequencies respectively, shows the significant difference between the mobilities of the carriers associated with two different Fermi pockets. The value of the quantum mobility in a system is always lower than the value of the classical Drude mobility (μ_c), as μ_q is sensitive to both large and small angle scattering, while μ_c is sensitive to only large angle scattering [37]. Therefore, the carrier mobility in ZrSiS are expected to be higher than the calculated values from quantum oscillation.

With magnetic field along **b** axis, no clear oscillation has been recorded within 9 T applied field. It may be due to heavier effective mass and low mobility of the charge carriers along that direction i.e. anisotropic nature of the Fermi surface.

To determine the nature of the charge carriers, as shown in Fig.5(b), Landau Level fan diagram for the larger Fermi pocket has been plotted, assigning maxima of the SdH oscillation as integers and minima as half integers. Extrapolated linear fitting gives an intercept of 0.15 (shown in the inset), which is very close to the ideal value $\pm 1/8$ for Dirac fermions. For 14.15 T Fermi pocket, however, the number of maxima and minima positions residing on a straight line is small within our experimental range of magnetic field. Therefore, we are unable to show the Landau index plot for the small Fermi pocket.

To determine the sign of the charge carriers from the two Fermi pockets, Hall effect measurement was performed at different temperatures. At 300 K the Hall resistance was found out to be almost linear with field and positive, which indicates holes as majority carriers. Earlier report at room temperature, also showed holes as majority carriers [27]. Upon decreasing the temperature, the Hall resistance develops a sublinear character indicating the presence of more than one type of carriers. Below around 50 K, the Hall resistance goes from positive to negative values at high magnetic fields. Thus the existence of more than one Fermi pocket is confirmed. The overall behavior of the Hall resistance can be understood by considering low mobility carriers associated with large Fermi pocket as hole type and and higher mobility carriers bound to small Fermi pocket as electron type. From the above, it is clear that at least two band crossings are present in electronic band structure of ZrSiS at different energy values, as shown in schematic Fig. 6(b).

The earlier report of ARPES and band structure calculations suggests, there are multiple Dirac crossings present in the system at different energy values as illustrated in the schematic Fig. 6(c). As shown, the Dirac cones 3 and 4 cross the Fermi energy, having Dirac points at two different energy values. Among others, 1 and 2 have their band crossing points almost at the chemical potential energy with negligible Fermi surface volume, while 5 and 6 lying at much lower energies. Thus in this configuration, it is expected that only signature of Dirac cones 3 and 4 will be observed in the transport properties of ZrSiS, which is consistent with our magneto-transport results.

In summery we report the magneto-electronic transport properties of ZrSiS single crystals. Magnetic field induced metal-semiconductor crossover along with a strong anisotropy with applied field direction, have been observed. Extremely large, non linear transverse MR, with

a value $\sim 1.4 \times 10^5$ % at 2 K and 9 T has been obtained, without any signature of saturation. Analyzing SdH oscillation we have found two inequivalent Fermi surface cross-sections perpendicular to crystallographic **c** axis. Fermi velocity, Fermi momentum and cyclotron

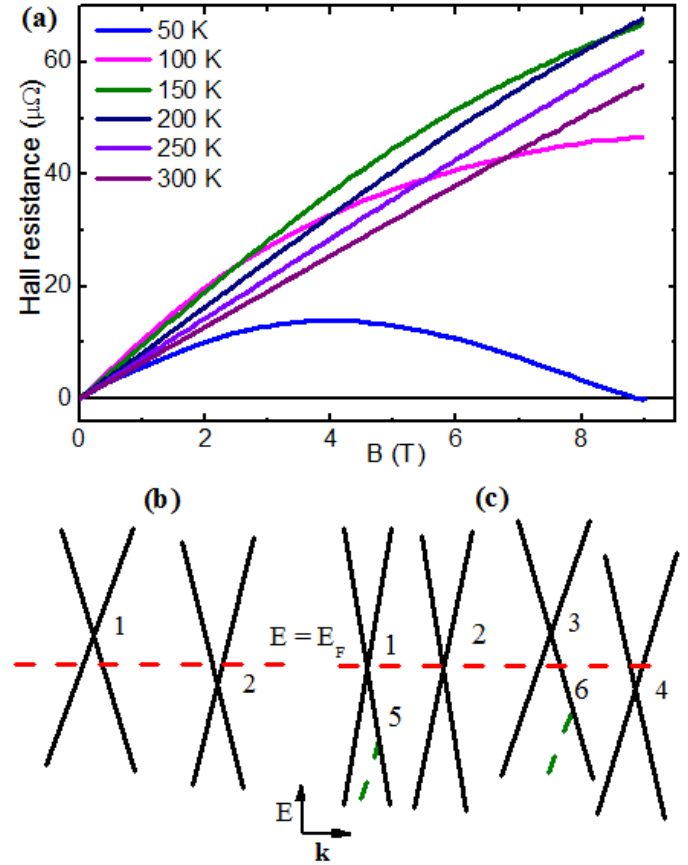


FIG. 6. (a) Field dependence of Hall resistance measured at different temperatures. (b) Schematic explaining transport measurement results. (c) Schematic illustrating multiple Dirac cones in ZrSiS as described in earlier report [27].

effective mass have been calculated from the oscillation in transport properties. The presence of Dirac fermions in the system is confirmed from the calculated non-trivial π Berry phase. Non-linear field dependence of Hall resistance indicates the presence of both electron and hole type of carriers in the system. SdH oscillation along with Hall measurement reflect multiple band crossings at different energy values of band structure, as reported earlier in first principle and ARPES measurement.

Acknowledgement: We thank N. Khan, A. Paul and S. Roy for their help during measurements and useful discussions.

[1] M. Z. Hasan, C. L. Kane, Rev. Mod. Phys. **82**, 3045 (2010).

[2] X. L. Qi, S. C. Zhang, Rev. Mod. Phys. **83**, 1057 (2011).

- [3] C. L. Kane, E. J. Mele, Phys. Rev. Lett. **95**, 146802 (2005).
- [4] L. Fu, C. L. Kane, E. J. Mele, Phys. Rev. Lett. **98**, 106803 (2007).
- [5] Y. L. Chen, J. G. Analytis, J.-H. Chu, Z. K. Liu, S.-K. Mo, X. L. Qi, H. J. Zhang, D. H. Lu, X. Dai, Z. Fang, S. C. Zhang, I. R. Fisher, Z. Hussain, Z.-X. Shen, Science **325**, 178 (2009).
- [6] Z. Wang, Y. Sun, X.-Q. Chen, C. Franchini, G. Xu, H. Weng, X. Dai, Z. Fang, Phys. Rev. B **85**, 195320 (2012).
- [7] Z. Wang, H. Weng, Q. Wu, X. Dai, Z. Fang, Phys. Rev. B **88**, 125427 (2013).
- [8] M. Neupane, S. Y. Xu, R. Sankar, N. Alidoust, G. Bian, C. Liu, I. Belopolski, T. R. Chang, H. T. Jeng, H. Lin, A. Bansil, F. Chou, M. Z. Hasan, Nat. Commun. **5**, 3786 (2014).
- [9] Y. Zhao, H. Liu, C. Zhang, H. Wang, J. Wang, Z. Lin, Y. Xing, H. Lu, J. Liu, Y. Wang, S. M. Brombosz, Z. Xiao, S. Jia, X. C. Xie, J. Wang, Phys. Rev. X **5**, 031037 (2015).
- [10] J. Cao, S. Liang, C. Zhang, Y. Liu, J. Huang, Z. Jin, Z. G. Chen, Z. Wang, Q. Wang, J. Zhao, S. Li, X. Dai, J. Zou, Z. Xia, L. Li, F. Xiu, Nat. Commun. **6**, 7779 (2015).
- [11] Z. K. Liu, B. Zhou, Y. Zhang, Z. J. Wang, H. M. Weng, D. Prabhakaran, S. K. Mo, Z. X. Shen, Z. Fang, X. Dai, Z. Hussain, Y. L. Chen, Science **343**, 864 (2014).
- [12] S.-Y. Xu, I. Belopolski, N. Alidoust, M. Neupane, C. Zhang, R. Sankar, S. - M. Huang, C.- C. Lee, G. Chang, B. Wang, G. Bian, H. Zheng, D. S. Sanchez, F. Chou, H. Lin, S. Jia, M. Z. Hasan, Science **349**, 613 (2015).
- [13] X. Huang, L. Zhao, Y. Long, P. Wang, D. Chen, Z. Yang, H. Liang, M. Xue, H. Weng, Z. Fang, X. Dai, G. Chen, Phys. Rev. X **5**, 031023 (2015).
- [14] C. Shekhar, A. K. Nayak, Y. Sun, M. Schmidt, M. Nicklas, I. Leermakers, U. Zeitler, Y. Skourski, J. Wosnitza, Z. Liu, Y. Chen, W. Schnelle, H. Borrmann, Y. Grin, C. Felser, B. Yan, Nat. Phys. **11**, 645 (2015).
- [15] J. Hu, J.Y. Liu, D. Graf, S.M.A Radmanesh, D.J. Adams, A. Chuang, Y. Wang, I. Chiorescu, J. Wei, L. Spinu, Z. Q. Mao, Scien. Reports **6**, 18674 (2016).
- [16] N. J. Ghimire, Y. Luo, M. Neupane, D. J. Williams, E. D. Bauer, F. Ronning, J. Phys. Cond. Matt. **27**, 152201 (2015).
- [17] S. Borisenko, D. Evtushinsky, Q. Gibson, A. Yaresko, T. Kim, M. N. Ali, B. Buechner, M. Hoesch, R. J. Cava, arXiv:1507.04847 (2015).
- [18] C. Fang, Y. Chen, H.-Y. Kee, L. Fu, Phys. Rev. B **92**, 081201(R) (2015).
- [19] Y. Kim, B. J. Wieder, C. L. Kane, A. M. Rappe, Phys. Rev. Lett. **115**, 036806 (2015).
- [20] A. A. Burkov, M. D. Hook, L. Balents, Phys. Rev. B **84**, 235126 (2011).
- [21] C.-K. Chiu, A. P. Schnyder, Phys. Rev. B **90**, 205136 (2014).
- [22] R. Yu, H. Weng, Z. Fang, X. Dai, X. Hu, Phys. Rev. Lett. **115**, 036807 (2015).
- [23] L. S. Xie, L. M. Schoop, E. M. Seibel, Q. D. Gibson, W. Xie, R. J. Cava, Appl. Phys. Lett. Mater. **3**, 083602 (2015).
- [24] G. Bian, T.-R. Chang, H. Zheng, S. Velury, S.-Y. Xu, T. Neupert, C.-K. Chiu, S.-M. Huang, D. S. Sanchez, I. Belopolski, N. Alidoust, P.-J. Chen, G. Chang, A. Bansil, H.-T. Jeng, H. Lin, M. Z. Hasan, arXiv:1508.07521 (2015).
- [25] G. Bian, T.-R. Chang, R. Sankar, S.-Y. Xu, H. Zheng, T. Neupert, C.-K. Chiu, S.-M. Huang, G. Chang, I. Belopolski, D. S. Sanchez, M. Neupane, N. Alidoust, C. Liu, B. K. Wang, C.-C. Lee, H.-T. Jeng, C. Zhang, Z. Yuan, S. Jia, A. Bansil, F. Chou, H. Lin, M. Z. Hasan, Nat. Commun. **7**, 10556 (2016).
- [26] M. N. Ali, Q. D. Gibson, T. Klimczuk, R. J. Cava, Phys. Rev. B **89**, 020505(R) (2014).
- [27] L. M. Schoop, M. N. Ali, C. Straßer, V. Duppel, S. S. P. Parkin, B. V. Lotsch, C. R. Ast, arXiv:1509.00861 (2015).
- [28] A. K. Haneveld, F. Jellinek, Recueil des Travaux Chimiques des Pays-Bas **83**, 776 (1964).
- [29] See supplementary information for 'Titanic magnetoresistance and signature of non-degenerate Dirac band crossings in ZrSiS.' [Url will be provided by the publisher.]
- [30] M. N. Ali, J. Xiong, S. Flynn, J. Tao, Q. D. Gibson, L. M. Schoop, T. Liang, N. Haldolaarachchige, M. Hirschberger, N. P. Ong, R. J. Cava, Nature **514**, 205 (2014).
- [31] K. Wang, D. Graf, L. Li, L. Wang, C. Petrovic, Scien. Reports **4**, 7328 (2014).
- [32] J. Hu, T. F. Rosenbaum, Nat. Mat. **7**, 697 (2008).
- [33] T. Hirahara, Y. Sakamoto, Y. Saisyu, H. Miyazaki, S. Kimura, T. Okuda, I. Matsuda, S. Murakami, S. Hasegawa, Phys. Rev. B **81**, 165422 (2010).
- [34] T. Liang, Q. Gibson, M. N. Ali, M. Liu, R. J. Cava, N. P. Ong, Nat. Mat **14**, 280 (2015).
- [35] D. Shoenberg, Magnetic oscillations in metals, Cambridge Univ. Press, 1984.
- [36] J. Feng, Y. Pang, D. Wu, Z. Wang, H. Weng, J. Li, X. Dai, Z. Fang, Y. Shi, L. Lu, Phys. Rev B **92**, 081306(R) (2015).
- [37] A. Narayanan, M. D. Watson, S. F. Blake, N. Bruyant, L. Drigo, Y. L. Chen, D. Prabhakaran, B. Yan, C. Felser, T. Kong, P. C. Canfield, A. I. Coldea, Phys. Rev. Lett. **114**, 117201 (2015).

Supplementary information: Titanic magnetoresistance and signature of non-degenerate Dirac nodes in ZrSiS.

For crystal structure determination, single crystal electron diffraction along different zone axis have been done, using high resolution transmission electron microscopy (HRTEM) in FEI, TECNAI G² F30, S - TWIN microscope operating at 300 kV equipped with a GATAN Orius SC1000B CCD camera. From the diffraction data, interplanar spacing and subsequently Miller indices of the crystal planes have been extracted.

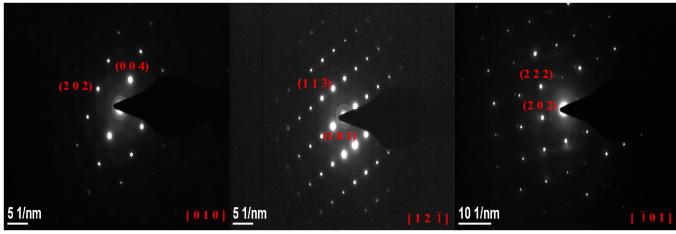


FIG. 7. Electron diffraction images of ZrSiS crystals with corresponding zone axis, obtained through HRTEM measurements.

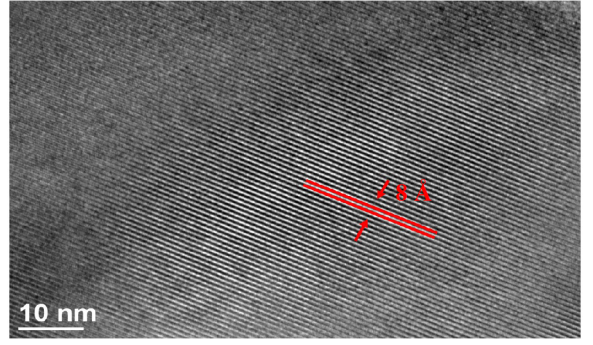


FIG. 8. HRTEM image along **ac** - plane.

To check the stoichiometry, we have performed Energy - dispersive X - ray (EDX) spectroscopy of the grown crystals using same microscope with a scanning unit and a high - angle annular dark - field scanning (HAADF) detector from Fischione (Model 3000). The obtained spectrum is shown in Fig. 9. Measured values are in very good agreement with the initial molar ratio of the starting elements.

The logarithmic behavior of resistivity with inverse temperature is shown in Fig. 10 with magnetic field applied along two different directions. Magnetic field induced metal - semiconductor transition is indicated by the change in the sign of the slope. From the slope of the curves thermal activation energy gaps have been calculated.

The calculated energy gaps exhibit magnetic field dependence for both directions of the applied fields.

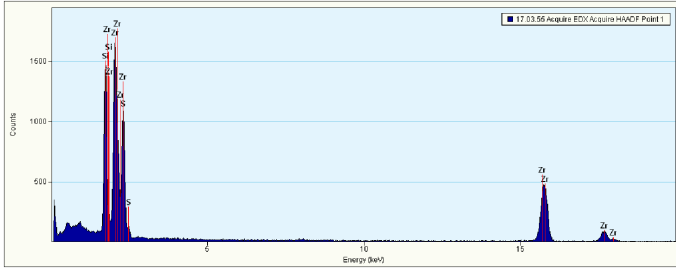


FIG. 9. Single crystal EDX spectroscopy data.

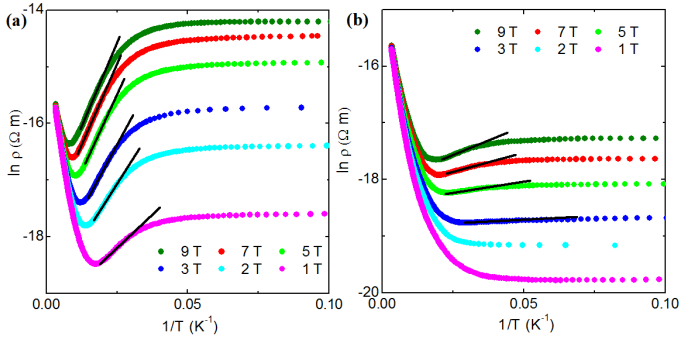


FIG. 10. $\ln(\rho)$ is plotted against T^{-1} at different transverse magnetic fields for (a) $B \parallel c$ - axis, (b) $B \parallel b$ - axis.

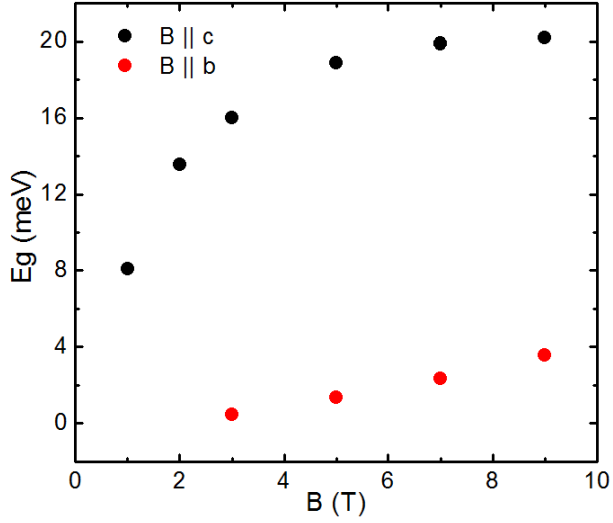


FIG. 11. Magnetic field dependence of calculated thermal energy gap for two different field directions.